

New material modeling approaches for thermoplastics, composites and organic sheet

Matthias Vogler, Consulting engineer, Hannover, Germany

vogler.consulting@email.de

Abstract: In this paper, new anisotropic elastic-viscoplastic constitutive models for simulating thermoplastic materials, endless fiber reinforced composites and organic sheets are presented. The anisotropic material models address the same main features as the isotropic SAMP model (MAT_187 in LS-DYNA). These are in particular pressure dependent yielding allowing for different yielding in tension, compression, shear and biaxial loadings, tabulated input of hardening data for each stress state and a non-associated flow rule for a correct prediction of the volumetric plastic strains. Hence, the anisotropic material models represent a consistent further development of the isotropic SAMP material model (SAMP-1 or MAT_187 in LS-DYNA 971).) The anisotropy is incorporated by an invariant formulation using structural tensors. This provides interesting modeling techniques for short fiber reinforced thermoplastics and for organic sheets. When modeling short fiber reinforced thermoplastics, the fiber orientation tensor is directly integrated into the constitutive equations and an automated homogenization is performed. That is, the fiber orientation tensor "weights" the structural tensors representing the preferred directions and in the limiting case "all fiber directions equally distributed in all directions", the isotropic SAMP model is recovered as a special case. When modeling organic sheets, the finite fiber rotations observed under certain loading conditions can be simulated. That is, an initial misalignment of the yarns due to the draping process and also a loading induced misalignment of the yarns due to the forming process can be incorporated easily, letting the structural tensors rotate against each other.

The applicability of the anisotropic material models will be shown with three examples. First, simulation results of a short fiber reinforced polymer PA6GF60 are presented. These are in particular the material characterization tests (tensile, compression and shear tests) and quasi-static and dynamic 4a-Impetus bending tests. Secondly, simulation results of quasi-static and dynamic off-axis compression tests of a carbon epoxy IM7-8552 are presented, predicting the experimentally observed pre-failure nonlinearities. Finally, the applicability of the anisotropic model to organic sheets is discussed. The experimentally observed highly non-linear behavior under shear dominated loadings due to the finite fiber rotations and the quasi brittle behavior in uniaxial tension and compression in the main directions can be predicted. In future developments, the whole process chain drape simulation, forming simulation and crash simulation will be addressed.

1 Introduction

The effective use of polymer composite materials in aerospace and automotive structures relies on the ability to predict the ultimate load and residual strength of these structures. However, accurate failure predictions are only possible if the stress states for general loading conditions, boundary conditions and load histories are properly defined. Therefore, an accurate representation of the constitutive response of the composite material under multiaxial loading conditions, including high hydrostatic pressures, is required.

The pre-failure nonlinearities due to yielding of the epoxy resin can lead to a redistribution of stresses in a laminate and affect the onset of the ply failure mechanisms (matrix cracking, fiber-matrix pull-out, fiber failure). In particular, fiber matrix composites exhibit pronounced nonlinearities in shear dominated loadings, but also in uniaxial compression transverse to the fibers and in biaxial stress states distinct nonlinearities are observed. The necessity of regarding all these nonlinearities prior to the onset of cracking has been investigated and confirmed by several authors [10],[11]. However, sophisticated material models, which are able to capture all these nonlinearities under multiaxial

loading conditions and high triaxiality do not exist. Furthermore, most of the available models are only valid for the plane stress state.

The objective of this paper is to present fully three-dimensional anisotropic elastic-viscoplastic constitutive models for composite materials, which are able to regard all the plasticity based nonlinearities under multiaxial loading conditions. The transversely isotropic plasticity model proposed in this paper is used in combination with an invariant based quadratic failure criterion [1]. A schematic representation of the plasticity model coupled with a new smeared crack model [4] is shown in Fig.1.

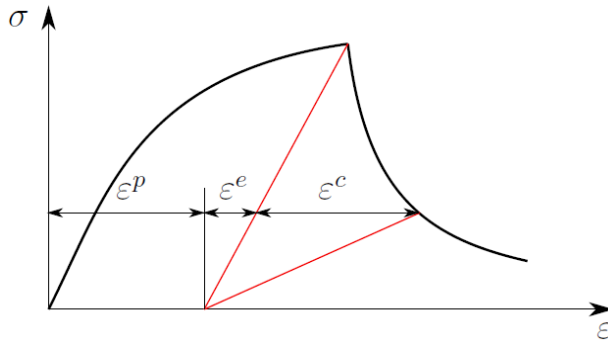


Fig. 1: Schematic representation of uniaxial stress-strain response for UD composites

The material behavior prior to the onset of cracking is governed by the elastic-(visco)plastic stress-strain relations, addressed in this paper. The onset and propagation of failure is governed by a smeared crack model, presented in [4].

Furthermore, anisotropic elastic-viscoplastic constitutive models for modeling short fiber reinforced thermoplastics and organic sheets are presented. The proposed phenomenological modeling approach for short fiber reinforced thermoplastics regards the fiber orientation tensor directly in the constitutive equations. Due to the formulation using structural tensors, a coordinate system free description of anisotropy is achieved and data from the mold flow simulation can be directly used in the material law.

The anisotropic material model for organic sheets regards finite fiber rotations. The effect of evolving anisotropy due to the reorientation of the yarns can be modeled while letting rotate the vectors of the preferred directions (yarn directions) against each other. With this modeling approach, initial and loading induced yarn rotations can be predicted. Furthermore, the experimentally observed stiffening effect in $\pm 45^\circ$ tensile tests can be modeled phenomenologically.

2 Kinematics

The elastic-viscoplastic constitutive models presented in Sec.3 are implemented in commercial finite element codes via user interfaces and user elements, both for implicit and explicit time integration. The kinematics used for large deformation regarding finite fiber rotations are explained hereafter.

2.1 Implicit framework

The kinematics for the implicit framework used for programming the material models presented in Sec.3 is based on a proposal of [12], which is presented hereafter. The deformation gradient $\mathbf{F}(\mathbf{X}, t)$ maps the initial configuration onto the current configuration:

$$\mathbf{F}(\mathbf{X}, t) = \frac{\partial \mathbf{x}}{\partial \mathbf{X}} \Big|_t = \mathbf{x} \overset{\leftarrow}{\nabla}_0 \quad (1)$$

and can be decomposed into a stretch tensor and a subsequent rotation or vice versa. The split is commonly performed using a polar decomposition and results in a symmetrical stretch tensor. An alternative decomposition which is more convenient when considering anisotropic materials is proposed by [12]. The symmetry condition of the stretch tensor is abandoned [12]. The deformation tensor is decomposed into a stretch tensor \mathbf{G} and a subsequent rotation \mathbf{R} :

$$\mathbf{F} = \mathbf{R} \cdot \mathbf{G}. \quad (2)$$

An arbitrary orthonormal rotation tensor \mathbf{R} can be chosen in (2) such that the non-symmetrical stretch tensor \mathbf{G} is invariant under rigid body rotations. With the decomposition (2), the velocity gradient \mathbf{L} is written as

$$\mathbf{L} = \mathbf{v} \overleftarrow{\nabla} = \dot{\mathbf{F}} \cdot \mathbf{F}^{-1} = \dot{\mathbf{R}} \cdot \mathbf{R}^T + \mathbf{R} \cdot \dot{\mathbf{G}} \cdot \mathbf{G}^{-1} \cdot \mathbf{R}^T, \quad (3)$$

where \mathbf{v} is the velocity. Introducing the tensors $\boldsymbol{\Omega}$ and \mathbf{L}^G as

$$\begin{aligned} \boldsymbol{\Omega} &= \dot{\mathbf{R}} \cdot \mathbf{R}^T, \\ \mathbf{L}^G &= \dot{\mathbf{G}} \cdot \mathbf{G}^{-1}, \end{aligned} \quad (4)$$

the velocity gradient is split into the skew symmetric spin tensor $\boldsymbol{\Omega}$ and an invariant non-symmetric rate of deformation tensor:

$$\mathbf{L} = \boldsymbol{\Omega} + \mathbf{R} \cdot \mathbf{L}^G \cdot \mathbf{R}^T. \quad (5)$$

The tensor $\boldsymbol{\Omega}$ is equal to the spin tensor \mathbf{W} , if the stretch tensor is symmetric. The second term of (5) is then equal to the symmetric rate of deformation tensor \mathbf{D} :

$$\mathbf{L} = \mathbf{W} + \mathbf{D} = \frac{1}{2}(\mathbf{v} \overleftarrow{\nabla} - \overrightarrow{\nabla} \mathbf{v}) + \frac{1}{2}(\mathbf{v} \overleftarrow{\nabla} + \overrightarrow{\nabla} \mathbf{v}). \quad (6)$$

However, the decomposition of (2) does not necessarily result in a symmetric stretch tensor in which case $\boldsymbol{\Omega}$ and \mathbf{W} will differ, see [12] for further explanation. The rate of rotation tensor $\dot{\mathbf{R}}$ is found by rewriting (3):

$$\dot{\mathbf{R}} = \mathbf{L} \cdot \mathbf{R} - \mathbf{R} \cdot \dot{\mathbf{G}} \cdot \mathbf{G}^{-1} = \boldsymbol{\Omega} \cdot \mathbf{R}. \quad (7)$$

The local stress tensor is introduced as

$$\boldsymbol{\tau} = \mathbf{e}_i \cdot \boldsymbol{\tau}_{ij} \cdot \mathbf{e}_j, \quad (8)$$

With \mathbf{e}_i and \mathbf{e}_j being the global base vectors. The local stress tensor $\boldsymbol{\tau}$ co-rotates with the rigid body rotations of the axis of anisotropy. Consequently, the stress tensor $\boldsymbol{\tau}$ is invariant and is related to the global Cauchy stress tensor $\boldsymbol{\sigma}$ by a rotation only:

$$\boldsymbol{\sigma} = \mathbf{R} \cdot \boldsymbol{\tau} \cdot \mathbf{R}^T. \quad (9)$$

This approach was introduced by [13] and leads to a conceptually simple scheme for an updated or total Lagrange FE formulation for anisotropic materials. Nonlinearities due to reorientation of the material (yarns in a fabric) are taken into account when mapping the local stress tensor to the global Cauchy stress tensor.

The commonly used right and left Cauchy Green tensor, \mathbf{C} and \mathbf{B} respectively, can be rewritten using the decomposition (2):

$$\begin{aligned} \mathbf{C} &= \mathbf{F}^T \cdot \mathbf{F} = \mathbf{G}^T \cdot \mathbf{G}, \\ \mathbf{B} &= \mathbf{F} \cdot \mathbf{F}^T = \mathbf{R} \cdot \mathbf{G} \cdot \mathbf{G}^T \cdot \mathbf{R}^T. \end{aligned} \quad (10)$$

The rate of the right Cauchy Green tensor is related to the rate of deformation tensor \mathbf{D} according to

$$\dot{\mathbf{C}} = 2\mathbf{F}^T \cdot \mathbf{D} \cdot \mathbf{F} = 2\mathbf{G}^T \cdot \mathbf{R}^T \cdot \mathbf{D} \cdot \mathbf{R} \cdot \mathbf{G}. \quad (11)$$

The rate of the Cauchy stress is related to the local stress and the local stress rate:

$$\dot{\boldsymbol{\sigma}} = \dot{\mathbf{R}} \cdot \boldsymbol{\tau} \cdot \mathbf{R}^T + \mathbf{R} \cdot \dot{\boldsymbol{\tau}} \cdot \mathbf{R}^T + \mathbf{R} \cdot \boldsymbol{\tau} \cdot \dot{\mathbf{R}}^T. \quad (12)$$

For the elastic-plastic material models, the total deformation is split into an elastic reversible part and a plastic irreversible part:

$$\mathbf{F} = \mathbf{R} \cdot \mathbf{G}_e \cdot \mathbf{G}_p. \quad (13)$$

This results in a split of the velocity gradient \mathbf{L}^G in an elastic part \mathbf{L}_e and in a plastic part \mathbf{L}_p

$$\mathbf{L}^G = \mathbf{L}_e + \mathbf{L}_p, \quad (14)$$

with

$$\begin{aligned} \mathbf{L}_e &= \dot{\mathbf{G}} \cdot \mathbf{G}_e^{-1} \\ \mathbf{L}_p &= (\mathbf{G}_e \cdot \mathbb{I} \cdot \mathbf{G}_e^{-T}) : \dot{\mathbf{G}}_p \cdot \mathbf{G}_p^{-1} \end{aligned} \quad (15)$$

Where \mathbb{I} is the fourth order identity tensor. The proposed kinematics is implemented in Abaqus and FEAP user elements.

2.2 Explicit framework

The rate constitutive equations are often used in finite element analyses at large strains. These rate constitutive equations are written in the current configuration. Since hyperelastic-plastic constitutive equations are generally written in the initial configuration, they are inappropriate in the case of large strains as they occur in fabrics. The proposed rate constitutive equations are a good choice for history dependent material behavior such as elasto-plasticity in an explicit framework. The so called objective stress rate is the derivative for an observer who is fixed with respect to the material. Since this requirement is not uniquely defined, there are several objective derivatives.

The rate constitutive equation has the form

$$\boldsymbol{\sigma}^\nabla = \mathbf{C} : \mathbf{D} \quad (16)$$

with

$$\boldsymbol{\sigma}^\nabla = \mathbf{Q} \left(\frac{d}{dt} (\mathbf{Q}^T \cdot \boldsymbol{\sigma} \mathbf{Q}) \right) \mathbf{Q}^T = \dot{\boldsymbol{\sigma}} + \boldsymbol{\sigma} \cdot \boldsymbol{\Omega} - \boldsymbol{\Omega} \cdot \boldsymbol{\sigma} \quad (17)$$

$\boldsymbol{\Omega}$ is the spin corresponding to \mathbf{Q} :

$$\boldsymbol{\Omega} = \dot{\mathbf{Q}} \cdot \mathbf{Q}^T \quad (18)$$

The most common objective derivatives are those of Green-Naghdi and Jaumann. In the case of the derivative of Green-Naghdi the rotation \mathbf{Q} considered as that of the material is the rotation of the polar decomposition:

$$\mathbf{Q} = \mathbf{R} \quad (19)$$

which is derived from the decomposition $\mathbf{F}=\mathbf{R}\cdot\mathbf{U}$ of the gradient tensor with \mathbf{R} being the polar rotation and \mathbf{U} being the right stretch tensor. In the case of the derivative of Jaumann, \mathbf{Q} is the rotation of the co-rotational spinless frame:

$$\mathbf{Q} = \mathbf{R}_s \quad (20)$$

which is derived from the velocity gradient and the spin

$$\boldsymbol{\Omega}_s = \frac{1}{2} (\nabla \mathbf{v} - \nabla^T \mathbf{v}) = \dot{\mathbf{R}}_s \cdot \mathbf{R}_s^T \quad (21)$$

In Abaqus explicit, the Jaumann objective derivatives are used. In LS-DYNA, also the Jaumann objective rate is supposed to be used. However, differences occur under large rotations when comparing the solutions obtained with Abaqus explicit and LS-DYNA.

3 Elastic-viscoplastic constitutive models

To establish the constitutive equations for the anisotropic elastic-viscoplastic material models, the mathematical framework of invariant theory is used. This mathematical concept enables the representation of anisotropic constitutive equations as isotropic tensor functions [9], [7]. In this context, the anisotropy is not derived using symmetry conditions which refer to a reference coordinate system, but by structural tensors which represent the anisotropy as an intrinsic material property in a coordinate system free description. The structural tensors are formed by the dyadic product of the vectors of the preferred direction, \mathbf{a} and \mathbf{b} . Due to some additional constraints, one direction is redundant and the structural tensors which have to be regarded for orthotropy and monoclinic anisotropy are:

$$\mathbf{A} := \mathbf{a} \otimes \mathbf{a}, \quad \mathbf{B} := \mathbf{b} \otimes \mathbf{b} \quad (22)$$

In case of transversely isotropic behaviour, just one structural tensor is required. A detailed description of deriving constitutive equations in the format of isotropic tensor function is found in [9],[7] and [8].

In case of monoclinic behaviour, the 4th order elasticity tensor reads:

$$\begin{aligned} \mathbf{C} = & \lambda \mathbf{1} \otimes \mathbf{1} + 2\mu \mathbb{I} + \alpha_1 (\mathbf{A} \otimes \mathbf{1} + \mathbf{1} \otimes \mathbf{A}) + \alpha_2 (\mathbf{B} \otimes \mathbf{1} + \mathbf{1} \otimes \mathbf{B}) \\ & + 2\mu_1 \mathbb{I}_A + 2\mu_2 \mathbb{I}_B \\ & + \beta_1 \mathbf{A} \otimes \mathbf{A} + \beta_2 \mathbf{B} \otimes \mathbf{B} + \beta_3 (\mathbf{A} \otimes \mathbf{B} + \mathbf{B} \otimes \mathbf{A}) \\ & + \beta_4 (\mathbf{AB} \otimes \mathbf{AB} + \mathbf{AB} \otimes \mathbf{AB}) + \dots \end{aligned} \quad (23)$$

In case the elasticity parameter β_4 is zero, orthotropy is comprised as a special case. The orthotropic elasticity tensor with 9 independent elasticity parameters reads in matrix notation:

$$\mathbf{C} = \begin{bmatrix} \lambda + 2\mu & \lambda + \alpha_1 & \lambda + \alpha_2 & 0 & 0 & 0 \\ \lambda + \alpha_1 & \lambda + 2\mu + 2\alpha_1 & \lambda + \alpha_1 + \alpha_2 + \beta_3 & 0 & 0 & 0 \\ \lambda + \alpha_2 & \lambda + \alpha_1 + \alpha_2 + \beta_3 & \lambda + 2\mu + 2\alpha_2 & 0 & 0 & 0 \\ 0 & 0 & 0 & \mu + \mu_1 & 0 & 0 \\ 0 & 0 & 0 & 0 & \mu + \mu_2 & 0 \\ 0 & 0 & 0 & 0 & 0 & \mu + \mu_1 + \mu_2 \end{bmatrix} \quad (24)$$

When modeling fabrics, the loading induced rotation of the yarns has to be regarded. That is, the effect of evolving anisotropy is modeled by a rotation of the vectors representing the preferred direction. If all three vectors are not perpendicular, the general case of triclinic anisotropy with 21 independent constants is obtained [8]. In case the third vector \mathbf{c} is still perpendicular to the yarn vectors \mathbf{a} and \mathbf{b} , the special case of monoclinic anisotropy with 13 independent elasticity constants is obtained. The decisive parameter is the monoclinic elasticity parameter β_4 in (23). The corresponding mixed invariant \mathbf{AB} is just active in case not ($\mathbf{a} \perp \mathbf{b}$). Consequently, the parameter β_4 just takes effect in case the yarns angle is unequal to 90° - otherwise, the orthotropic case is recovered. The parameter β_4 accounts for a normal load – shear interaction as highlighted in (23) and (24) (red color). The effect of the parameter β_4 is studied in Sec.4.3.

The anisotropic yield surface and plastic potential formulations presented hereafter can be summarized using 4th and 2nd order tensors. Since an anisotropic hardening formulation is used, the equivalent plastic strain is an argument of the yield surface formulation. The generalized form of the yield surface formulation reads:

$$f(\boldsymbol{\sigma}, \mathbf{A}, \mathbf{B}, \bar{\varepsilon}^p) = \frac{1}{2}\boldsymbol{\sigma} : \mathbb{K} : \boldsymbol{\sigma} + \mathbf{L} : \boldsymbol{\sigma} - 1 . \quad (25)$$

The generalized form of the plastic potential formulation reads:

$$g(\boldsymbol{\sigma}, \mathbf{A}, \mathbf{B}) = \frac{1}{2}\boldsymbol{\sigma} : \mathbb{M} : \boldsymbol{\sigma} - 1 . \quad (26)$$

The viscoplastic formulation used is a Perzyna type overstress model:

$$\Delta\gamma_{n+1}^{vp} = \frac{\langle f_{n+1} \rangle^m}{\eta} \Delta t . \quad (27)$$

This formulation turned out to be very efficient from a numerical point of view. Furthermore, the determination of the two viscoplastic parameters m and η is quite easy and straight forward.

In order to formulate the invariant sets for transverse isotropy, orthotropy and for monoclinic anisotropy, a decomposition of the stress tensor according [9] into plasticity inducing stresses and stresses which cause elastic reactions is used:

$$\boldsymbol{\sigma} = \boldsymbol{\sigma}^{\text{pind}} + \boldsymbol{\sigma}^{\text{reac}} \quad (28)$$

With this decomposition, a decoupling of the invariants with respect to the stress states is achieved.

3.1 Transversely isotropic yield surface and plastic flow potential for UD composites

Transversely isotropic materials are characterized by a preferred direction \mathbf{a} , which is the fiber direction for unidirectional fiber composites. Thus, the material response is invariant with respect to arbitrary rotations around this preferred direction \mathbf{a} , to reflections at fiber parallel planes, and with respect to the reflection at that plane, whose normal is \mathbf{a} . These are the group of symmetry transformations for transverse isotropy. The structural tensor \mathbf{A} defined in (22) is used as an additional tensor argument to formulate the elastic free energy density, the yield function and the plastic potential as isotropic tensor functions.

Before the transversely isotropic invariants are formulated, the stress tensor is decomposed into plasticity inducing stresses and elastic reaction stresses, see Eq.(28):

$$\begin{aligned} \boldsymbol{\sigma}^{\text{reac}} &= \frac{1}{2}(\text{tr } \boldsymbol{\sigma} - \mathbf{a}\boldsymbol{\sigma}\mathbf{a})\mathbf{1} - \frac{1}{2}(\text{tr } \boldsymbol{\sigma} - 3\mathbf{a}\boldsymbol{\sigma}\mathbf{a})\mathbf{A} , \\ \boldsymbol{\sigma}^{\text{pind}} &= \boldsymbol{\sigma} - \frac{1}{2}(\text{tr } \boldsymbol{\sigma} - \mathbf{a}\boldsymbol{\sigma}\mathbf{a})\mathbf{1} + \frac{1}{2}(\text{tr } \boldsymbol{\sigma} - 3\mathbf{a}\boldsymbol{\sigma}\mathbf{a})\mathbf{A} \end{aligned} \quad (29)$$

The invariant base for the transversely isotropic yield surface and plastic potential formulations reads:

$$\begin{aligned} I_1 &:= \frac{1}{2}\text{tr}(\boldsymbol{\sigma}^{\text{pind}})^2 - \mathbf{a}(\boldsymbol{\sigma}^{\text{pind}})^2\mathbf{a} , \\ I_2 &:= \mathbf{a}(\boldsymbol{\sigma}^{\text{pind}})^2\mathbf{a} , \\ I_3 &:= \text{tr } \boldsymbol{\sigma} - \mathbf{a}\boldsymbol{\sigma}\mathbf{a} . \\ I_4 &:= \frac{3}{2}\mathbf{a}\boldsymbol{\sigma}^{\text{dev}}\mathbf{a} . \end{aligned} \quad (30)$$

In Eq.(30), $\boldsymbol{\sigma}^{\text{dev}}$ is the stress deviator. The transversely isotropic yield surface formulation for UD composites reads:

$$f = \hat{f}(\sigma, \bar{\varepsilon}^p, A) = \alpha_1 I_1 + \alpha_2 I_2 + \alpha_3 I_3 + \alpha_{32} I_3^2 - 1 , \quad (31)$$

with

$$\begin{aligned} \alpha_3 &= \alpha_3^t, \alpha_{32} = \alpha_{32}^t \quad \text{if } I_3 > 0 \quad \text{and} \\ \alpha_3 &= \alpha_3^c, \alpha_{32} = \alpha_{32}^c \quad \text{if } I_3 \leq 0 . \end{aligned} \quad (32)$$

The proposed yield function results in 6 yield surface parameters that have to be determined. Each one of these parameters and the corresponding invariants are related to certain loading states: transverse shear, in-plane shear, uniaxial and biaxial transverse tension and uniaxial and biaxial transverse compression. Fig. 2 shows a schematic representation of the transversely isotropic yield surface in stress space. The highlighted points are the "trigger points" of the yield surface, in which yielding is controlled. That is, in each of these points, an initial yield stress and a hardening curve giving the yield stress vs. the corresponding plastic strain can be predetermined via tabulated data. Consequently, the yield surface parameters $\alpha(\dots)$ are a function of the equivalent plastic strain. This is explained in detail in [2].

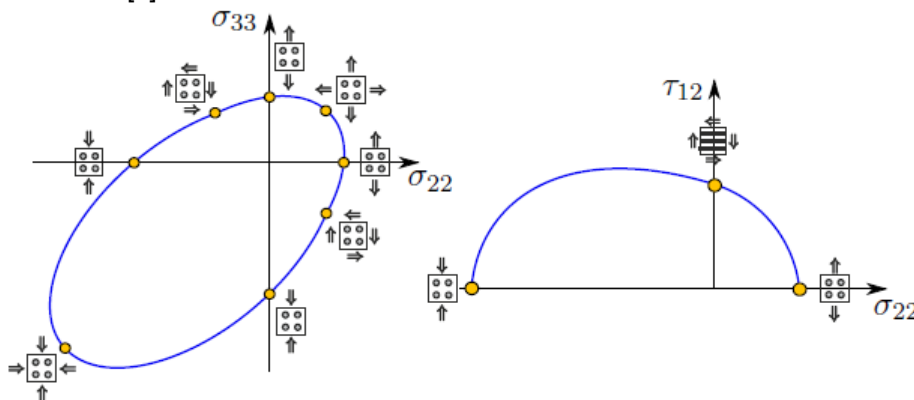


Fig. 2: Schematic representation of the transversely isotropic yield surface for UD composites in stress space

In order to obtain an accurate prediction of the plastic Poisson coefficients and of the volumetric plastic strains, a non-associated flow rule is used. That is, the evolution of the plastic strains is not given by the gradient of the yield surface, but by the gradient of a plastic potential function $g = g(\sigma, A)$. The plastic flow potential for unidirectional fiber reinforced polymers is similar to the yield surface formulation. However, the linear term I_3 is neglected. This has some advantages concerning the time integration as explained in [2]. The plastic potential formulation for UD composites reads:

$$g = \hat{g}(\sigma, A) = \beta_1 I_1 + \beta_2 I_2 + \beta_{32} I_3^2 - 1 . \quad (33)$$

The plastic potential function allows for controlling the plastic Poisson coefficients in uniaxial tension and compression transverse to the fibers. The determination of the plastic potential parameters β_1 , β_2 and β_{32} with the objective to represent a certain Poisson ratio is explained in detail in [2].

3.2 Orthotropic yield surface and flow potential for short fiber reinforced thermoplastics

The stress decomposition in order to compose the orthotropic invariants reads [9]:

$$\sigma^{\text{reac}} = -p\mathbf{1} + T_a A + T_b B \quad (34)$$

$$\begin{aligned} \sigma^{\text{pind}} &= \sigma + p\mathbf{1} - T_a A - T_b B \\ &= \sigma - (\text{tr } \sigma - a\sigma a - b\sigma b)\mathbf{1} + (\text{tr } \sigma - 2a\sigma a - b\sigma b)A \\ &\quad + (\text{tr } \sigma - a\sigma a - 2b\sigma b)B \end{aligned} \quad (35)$$

with the hydrostatic pressure

$$p = -\text{tr } \sigma + a\sigma a + b\sigma b \quad (36)$$

and with the projections onto the preferred directions

$$\begin{aligned} T_a &= -\text{tr } \sigma + 2a\sigma a + b\sigma b, \\ T_b &= -\text{tr } \sigma + a\sigma a + 2b\sigma b. \end{aligned} \quad (37)$$

The complete set in order to formulate the orthotropic yield condition and plastic flow potential reads:

$$\begin{aligned} I_1 &:= \frac{1}{2} \text{tr } (\sigma^{\text{pind}})^2 - a(\sigma^{\text{pind}})^2 a - b(\sigma^{\text{pind}})^2 b, \\ I_2 &:= a(\sigma^{\text{pind}})^2 a, \\ I_3 &:= b(\sigma^{\text{pind}})^2 b, \\ I_4 &:= \text{tr } \sigma - a\sigma a - b\sigma b, \\ I_5 &:= \frac{3}{2} a\sigma^{\text{dev}} a, \\ I_6 &:= \frac{3}{2} b\sigma^{\text{dev}} b. \end{aligned} \quad (38)$$

The orthotropic yield surface formulation reads:

$$f = \alpha_1 I_1 + \alpha_2 I_2 + \alpha_3 I_3 + \alpha_4 I_4 + \alpha_{42} I_4^2 + \alpha_5 I_5 + \alpha_{52} I_5^2 + \alpha_6 I_6 + \alpha_{62} I_6^2 - 1. \quad (39)$$

The yield surface (39) contains 9 independent parameters. Consequently, 9 material tests are required in order to obtain the 9 α -parameters of the orthotropic yield surface formulation (39). This is done completely automatically inside the material routine. For the input file, just the 9 hardening curves and the 9 orthotropic elasticity parameters are required. The stress states in which yielding is regarded are summarized in Fig. 3

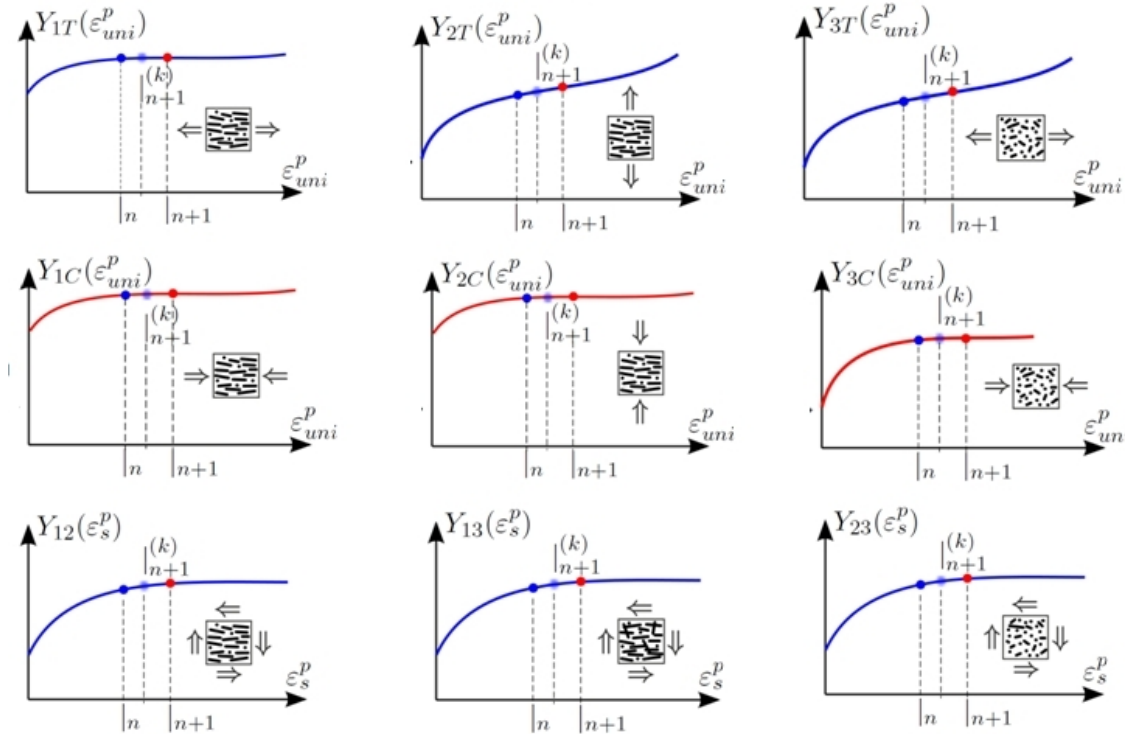


Fig. 3: Orthotropic yield surface formulation: Stress states in which yielding is controlled

The orthotropic plastic flow potential for short fiber reinforced thermoplastics is defined as:

$$g = \hat{g}(\sigma, A, B) = \beta_1 I_1 + \beta_2 I_2 + \beta_3 I_3 + \beta_4 I_4^2 + \beta_5 I_5^2 + \beta_6 I_6^2 - 1. \quad (40)$$

The orthotropic plastic flow potential enables a correct prediction of the plastic Poisson ratios in all three directions. The determination of the plastic flow parameters is not given here.

3.3 Anisotropic yield surface and flow potential for organic sheets

When modeling organic sheets, the orthogonality of the preferred directions \mathbf{a} and \mathbf{b} has to be abandoned and the more general case of monoclinic plasticity is assumed. Consequently, the invariant base used for the construction of the monoclinic yield surface and plastic potential formulation has to be extended with respect to the mixed invariant I_7 . Furthermore, for reasons of consistency the first three invariants of the orthotropic invariant set (38) has to be reformulated.

$$\begin{aligned} I_1 &:= \text{tr}(\sigma^{\text{pind}})^2 - \mathbf{a}(\sigma^{\text{pind}})^2 \mathbf{a} - \mathbf{b}(\sigma^{\text{pind}})^2 \mathbf{b} + \frac{1}{2} \text{tr}[\mathbf{A}\mathbf{B}(\sigma^{\text{pind}})^2] \\ I_2 &:= \mathbf{a}(\sigma^{\text{pind}})^2 \mathbf{a} - \text{tr}[\mathbf{A}\mathbf{B}(\sigma^{\text{pind}})^2] \\ I_3 &:= \mathbf{a}(\sigma^{\text{pind}})^2 \mathbf{a} - \text{tr}[\mathbf{A}\mathbf{B}(\sigma^{\text{pind}})^2] \\ I_7 &:= \text{tr}[\mathbf{A}\mathbf{B}(\sigma^{\text{pind}})^2] \end{aligned} \quad (41)$$

Note, that in case $\|\mathbf{a}\| = \|\mathbf{b}\| = 1 \wedge \mathbf{a} \perp \mathbf{b}$, the 7th invariant I_7 equals zero and the invariants I_1 , I_2 and I_3 are identical to the orthotropic invariants defined in (38). Based on the invariant set given in (41), the anisotropic yield surface formulation for modeling fabrics and organic sheets is defined:

$$f = \hat{f}(\boldsymbol{\sigma}, \bar{\varepsilon}^p, \mathbf{A}, \mathbf{B}) = \alpha_1 I_1 + \alpha_2 I_2 + \alpha_3 I_3 + \alpha_7 I_7 - 1 \quad (42)$$

The plastic flow potential for textile fabrics and organic sheets reads:

$$g = \hat{g}(\boldsymbol{\sigma}, \mathbf{A}, \mathbf{B}) = \beta_1 I_1 + \beta_2 I_2 + \beta_3 I_3 - 1 \quad (43)$$

The plastic flow potential allows for controlling the volumetric plastic strains. In the $\pm 45^\circ$ tests, a change in thickness is observed with growing yarn angels. This change in thickness can be exactly controlled with the β -parameters of the plastic flow potential.

4 Simulation results and modeling approaches

Hereafter, the modeling approaches and the simulation results for unidirectional endless fiber reinforced composites, for short fiber reinforced thermoplastics and for organic sheets are presented and discussed.

4.1 Quasi-static and dynamic off-axis compression tests for UD composites

First, the material data of the carbon-epoxy IM7-8552 are summarized. The material characterization based on the experimental data [6] and the determination of the material hardening curves is explained in detail in [2]. The elasticity parameters for IM7-8552 read:

	E_{11} [MPa]	E_{22} [MPa]	G_{12} [MPa]	ν_{12}	ν_{23}
IM7-8552	171420	8930	5100	0.0167	0.34
IM7-8552, red.	128000	6100	3800	0.0167	0.34

The strength parameters for IM7-8552 are:

	R_{\parallel}^t	R_{\parallel}^c	R_{\perp}^t	R_{\perp}^c	R_{\perp}^{bt}	R_{\perp}^{bc}	$R_{\parallel\perp}$	$R_{\perp\perp}$
IM7-8552	2326.0	1200.0	62.3	253.6	34.3	600.0	99.9	85.0

In Fig. 4 and Fig. 5 the derived hardening curves for carbon epoxy IM7-8552 are represented, see [2] for a detailed description. In both illustrations, the left-hand side shows the yield stress vs. corresponding plastic strains, the right-hand side shows stress vs. total strains. In Fig. 4, the in-plane and transverse shear hardening curves are given. Fig. 5 represents the hardening curves for uniaxial

and biaxial compression and uniaxial and biaxial tension. The cross represents the respective failure point in each stress state. In both the uniaxial and biaxial tensile hardening curve it can be seen that there are just minor pre failure nonlinearities. This is exactly that range, where a ductile-brittle transition of the material behavior occurs, see also Fig. 6.

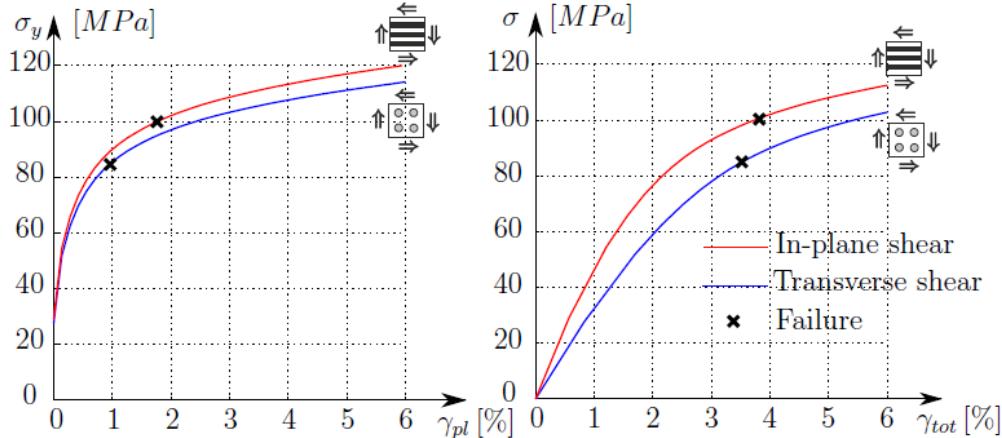


Fig. 4: Shear hardening behavior of IM7-8552 carbon-epoxy

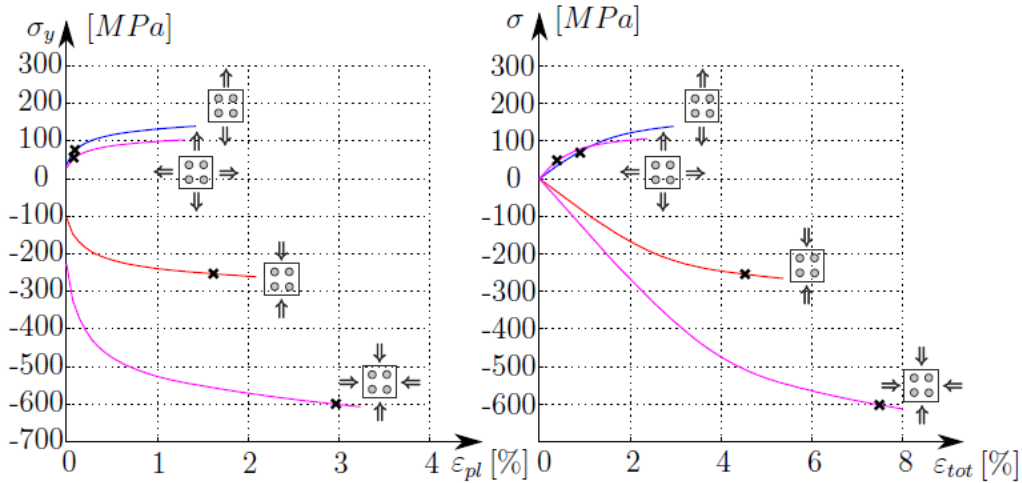


Fig. 5: Uniaxial and biaxial hardening behavior of IM7-8552 carbon-epoxy

Fig. 6 shows a representation of the yield surface (quasi-static), of the failure surface (quasi-static) and of the plastic potential in $I_3 - \sqrt{I_1}$ - invariant plane. The failure surface represents the failure criterion obtained with the IQC criterion presented in [1]. The concentric lines illustrate the yield surface at different loading histories. They represent an inflation of the yield surface due to the applied anisotropic hardening formulation.

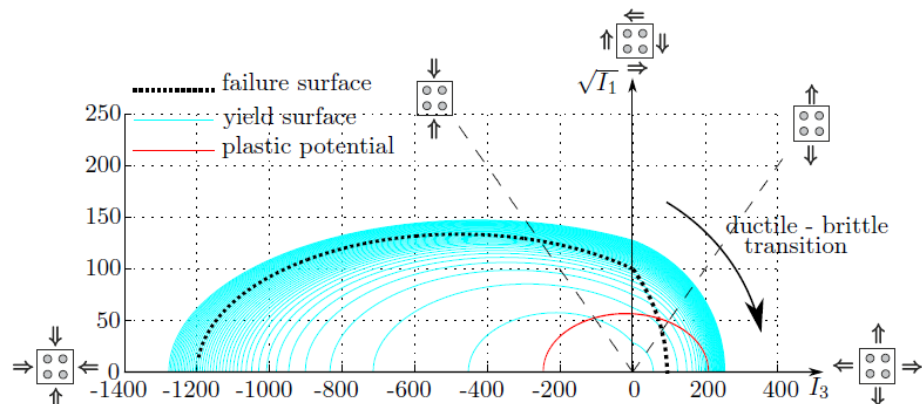


Fig. 6: Transversely isotropic yield surface for IM7-8552 in $I_3 - \sqrt{I_1}$ invariant plane

Fig. 7 shows the experimentally measured total Poisson ratio in the transverse compression test [6]. The evolution of the total Poisson ratio shows a saturation at a strain value of round about 4%. This is also the range where nearly all deformations are assumed to be plastic. As described in [2], a plastic Poisson ratio of 1.0 means incompressible behavior. For the current carbon-epoxy however, a plastic Poisson ratio of 0.8 is measured (see Fig. 7). Consequently, the assumption of incompressible behavior is not valid for fiber reinforced polymers. With respect to the simulation of the off-axis and transverse compression tests, the choice of the plastic Poisson ratio is not sensitive. However, the more confined the FE-model (respectively the real mechanical problem), the more sensitive is the choice of the plastic potential parameters. When simulating various laminate layups, it could be already shown that the plastic potential parameters (and hence the plastic Poisson ratios) are sensitive to the bending behavior. This has to be investigated in future developments. The determination of the β -parameters of the plastic potential formulation in order to predict the experimentally observed plastic Poisson ratio is described in detail in [2].

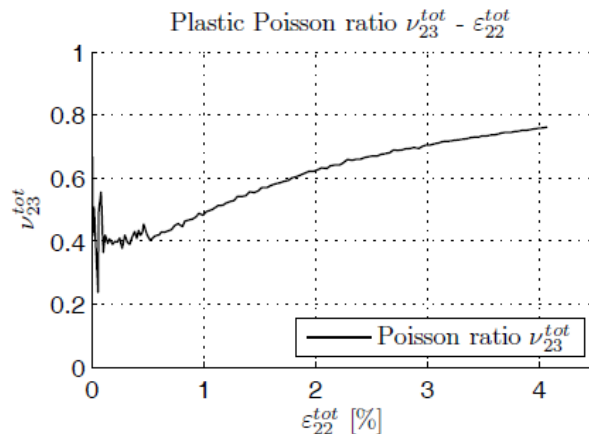


Fig. 7: Total Poisson ratio of IM7-8552, measured in the transverse compression test (90° - test)

According to the test program [6], off-axis compression tests with fiber angles $\theta = 15^\circ, 30^\circ, 45^\circ, 60^\circ$ and 75° and a transverse compression test ($\theta = 90^\circ$) are modeled and simulated. In order to study the mesh sensitivity, a single cubic element, a coarse mesh with 100 elements and a fine mesh with 800 elements are used, whereby the same boundary conditions as in the material tests are applied. That is, at the bottom the specimens are fixed whereas at the top (load application) the specimens can move in horizontal direction. In the experiments this is realized using a thin layer of Molybdenum-Disulfide (MoS_2). The layer of Molybdenum-Disulfide minimizes friction and allows a lateral deflection of the test specimen. The test specimen used by [6] and the corresponding FE discretizations showing the fine mesh, the coarse mesh and the single cubic element are represented in Fig. 8. Abaqus solid elements C3D8 are chosen for the spatial discretization. The simulations are performed both with Abaqus implicit (via user interface UMAT) and Abaqus explicit (via user interface VUMAT). Comparing the implicit and the explicit solution, no noticeable difference is observed between these two analysis methods, both for the simulation of the quasi-static and dynamic tests.

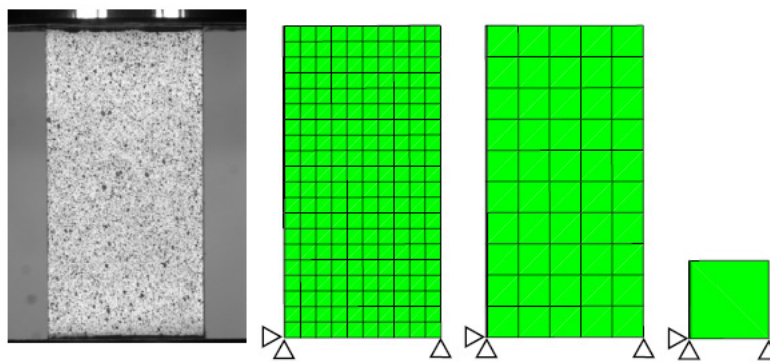


Fig. 8: Off-axis compression tests: Test specimen and FE-discretization

Before discussing these results, the mesh dependency of the numerical solutions is investigated exemplarily with the simulation of the quasi-static 45° off-axis compression test, see Fig. 9. Therefore, the 45° off-axis compression test is simulated with the fine mesh, with the coarse mesh and with the single element shown in Fig. 8. Comparing the results obtained with the coarse mesh and with the fine

mesh, absolutely no mesh dependency is observed, i.e. the simulated curves are nearly exactly coincident. However, the curve obtained with the single cubic element is a little bit higher than the curves predicted with the FE models with the two mesh refinements. The reason for this difference is probably a geometrical effect. Due to the difference in the geometry, the single cubic element exhibits a smaller tilting than the FE-Models with the coarse resp. fine mesh. This results in a slightly stiffer behavior of the single element. In contrast to the 45° off-axis test, the 90° transverse compression test does not show this difference between the single element and the FE-models (this is not illustrated here). That is, all three curves are coincident and absolutely no difference is observed. The reason for this behavior in the 90° test is that in contrast to the 45° off-axis test, the loading in the 90° test is applied into one of the main anisotropy directions and, consequently, no tilting of the specimen is observed, neither in the tests nor in the FE-simulations.

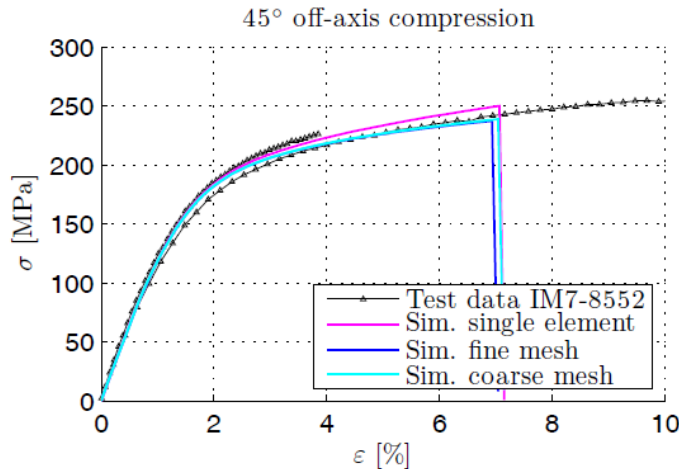


Fig. 9: Simulation results of the 45° quasi-static off-axis compression test with various mesh refinements

Fig. 10 shows the simulation off all off-axis and transverse compression tests and the comparison to the corresponding experimental data [6]. The black lines (marked with symbols) represent the experimental data, whereby the lower lines are the test data from the quasi-static tests and the upper lines represent the test data from the dynamic tests (strain rates round about 300 s^{-1}). The mesh dependency of the numerical solutions is already discussed above, based on the simulation of the 45° off axis tests. The discussion of the mesh dependency is representative for the simulations of all the other quasi-static and dynamic tests. Since no noticeable mesh dependency is observed, just simulations obtained with the coarse mesh (see Fig. 8) are represented in Fig. 10.

Considering the quasi-static off-axis simulations, a very good coincidence of the test data and the numerical predictions is observed in nearly all cases. Both the non-linear material behavior and the onset of failure are predicted very well. Just in the 60° quasi-static off axis compression test, the hardening behavior is slightly underestimated. An outcome of the experiments [6] is that there are homogenous stress and strain fields during load application both in the elastic and in the plastic regime. Just immediately before final failure occurs, localization in the fracture plane (the kink plane of the 15° off-axis test) is observed. This behavior is fully recovered in the simulations.

Considering the simulations of the dynamic tests, also a good agreement with the experiments is observed, see Fig. 10. Just in the 15° simulation and in the 30° simulation the experimentally measured curves are slightly overpredicted. In the 90°, 75°, 60° and 45° dynamic simulations the initial slope is a little bit underestimated. The reason for this is that also the elastic properties are rate dependent. This is not regarded in the constitutive model so far. For the strain rate range addressed in the off-axis tests, this drawback is tolerable. However, with respect to higher strain rates, this effect is supposed to be more dominant and rate effects on the elastic properties should be regarded in the constitutive model as well. Furthermore, it is understood that the two strain rate regimes (quasi static and dynamic) considered in the off-axis compression tests are not sufficient for an overall characterization at higher strain rate regimes. As already reported in [6], experimental evidence suggests that a shift from approximately linear to exponential strain rate behavior occurs between 100s^{-1} and 1000s^{-1} with significant increases of modulus and strength above 1000s^{-1} . However, up to the strain rate regimes considered in the available off-axis tests (i.e. 300 s^{-1}), the strain rate effects

are approximately linear and the applied Perzyna type viscoplastic formulation is sufficient in order to model the dynamic off-axis tests.

Interesting simulation results of triaxial tests performed by [5] are presented in [2]. These are in particular uniaxial compression tests of 45° and 90° UD specimens under various levels of hydrostatic pressures. In a first step, the hydrostatic pressure environment is imposed. In a second step, uniaxial compression is applied to the specimens. Due to the high hydrostatic pressure, the glass transition temperature drops from 80°C to operating temperature which results in pronounced yielding behavior and a decrease of the elasticity parameters. The behavior under high pressures can be approximated with the proposed yield surface formulation for UD composites Eq.(31), Eq.(32). Especially the assumed biaxial compression hardening behavior turned out to be very sensitive when modeling the triaxial tests.

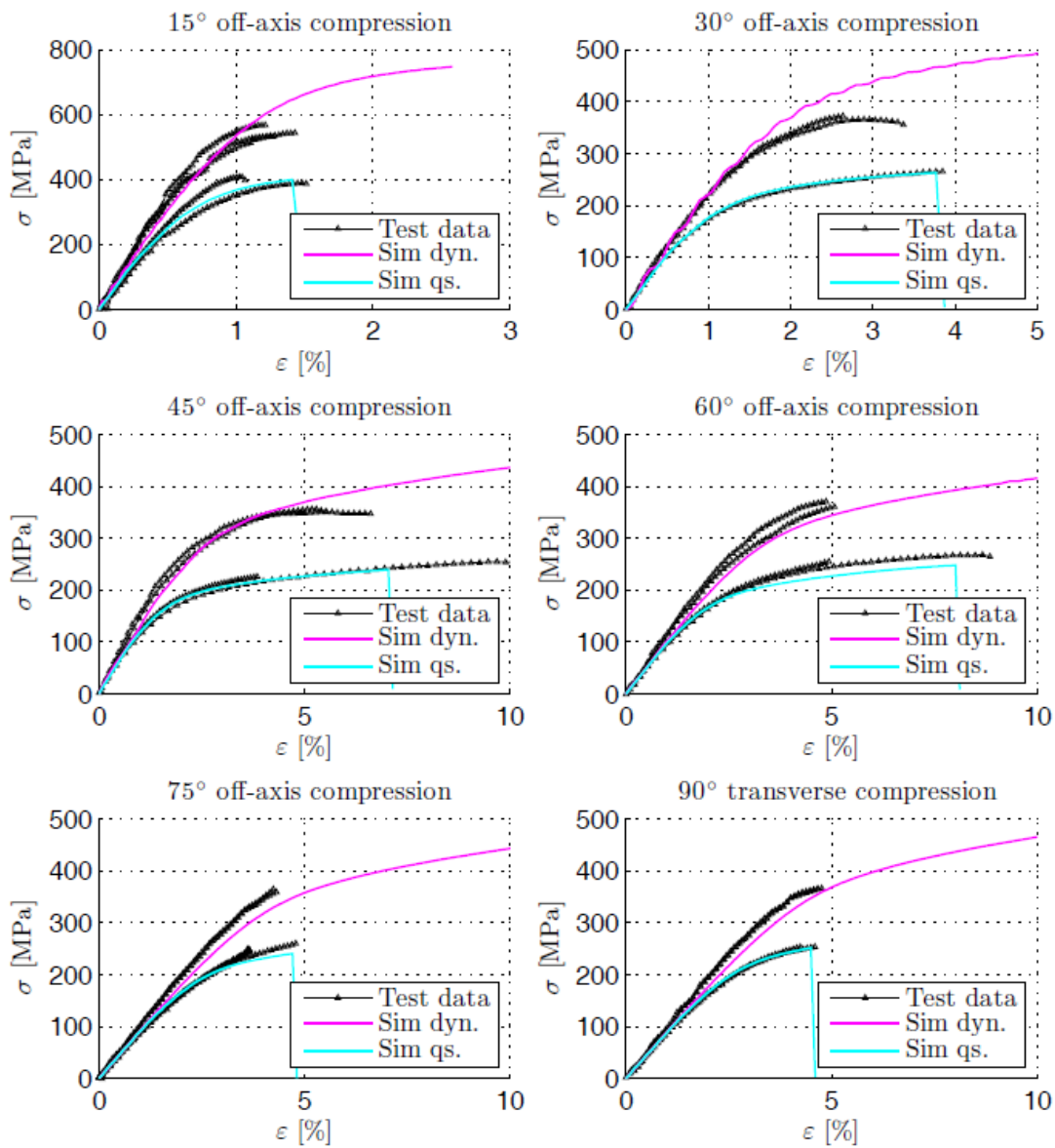


Fig. 10: Simulation of quasi-static and dynamic off-axis and transverse compression tests for unidirectional carbon-epoxy IM7-8552

4.2 Modeling short fiber reinforced thermoplastics

Hereafter, just the phenomenological modeling approach for modeling short fiber reinforced thermoplastics is presented. The simulation results of the material tests of PA6GF60 are already published in [3] in and will be shown in the presentation.

When modeling short fiber reinforced thermoplastics with the orthotropic material model presented in 3.2, the fiber orientation tensor can be directly regarded in the constitutive model. The main directions of the fiber orientation tensor are used in order to “weight” the structural tensors representing the main anisotropy directions. The typical layered structure due to the injection molding process is shown in Fig. 11. For modeling the 4a Impetus bending tests (see FE discretization in Fig. 12), two modeling approaches are chosen as represented in Fig. 13. In modeling variant 1, the fiber distribution is averaged over the whole cross section. In the modeling variant 2, the experimentally measured fiber distribution is regarded more precisely as shown in Fig. 13 (right hand side). Since the material characterization tests are just performed for the “averaged configuration”, the material behavior for the outer layers (fiber orientation configuration 80% / 20%) and for the inner layer (60% / 40%) is assumed based on a simple interpolation, respectively, extrapolation. This is schematically shown in Fig. 14. Since the principle axis of the fiber orientation tensor coincide with the preferred directions which compose the structural tensors Eq.(22), a coordinate system free description of anisotropy is achieved using the fiber orientation tensor as a “weighting function” for the structural tensors. This represents a very efficient phenomenological modeling approach for short fiber reinforced thermoplastics. Moreover, the fiber orientation tensor provided in the mold flow simulation can be directly used in the material model. The scheme of the proposed phenomenological modeling approach is shown in Fig. 15.

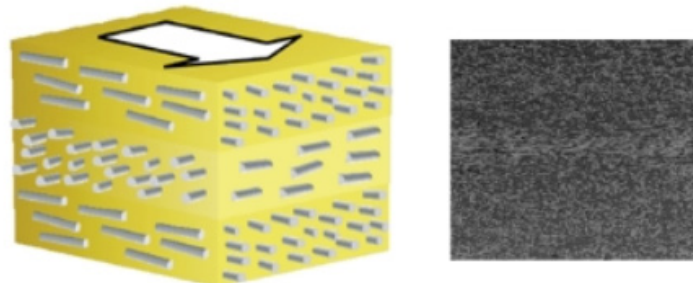


Fig. 11: Typical fiber distribution in an injection molded plate due to the mold flow process: schematic representation (left hand side) and ct scan

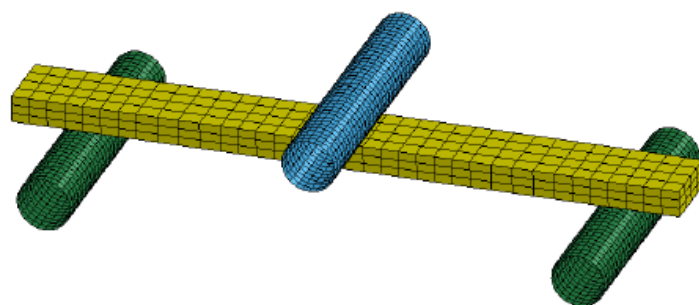


Fig. 12: FE discretization of 4a Impetus bending test

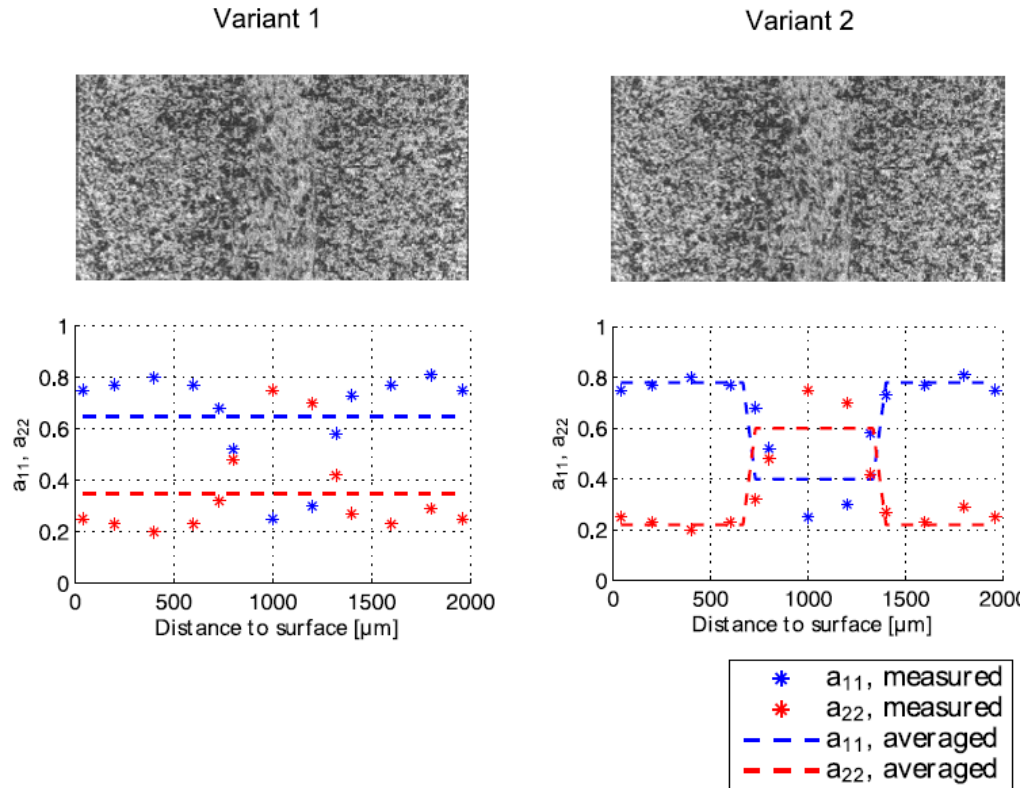


Fig. 13: Simulation variants for 4a Impetus bending test: variant 1- fiber distribution averaged over the cross section, variant 2 - fiber distribution averaged per layer. a_{11} and a_{22} are the components of the 2D fiber orientation tensor (no orientation in thickness direction)

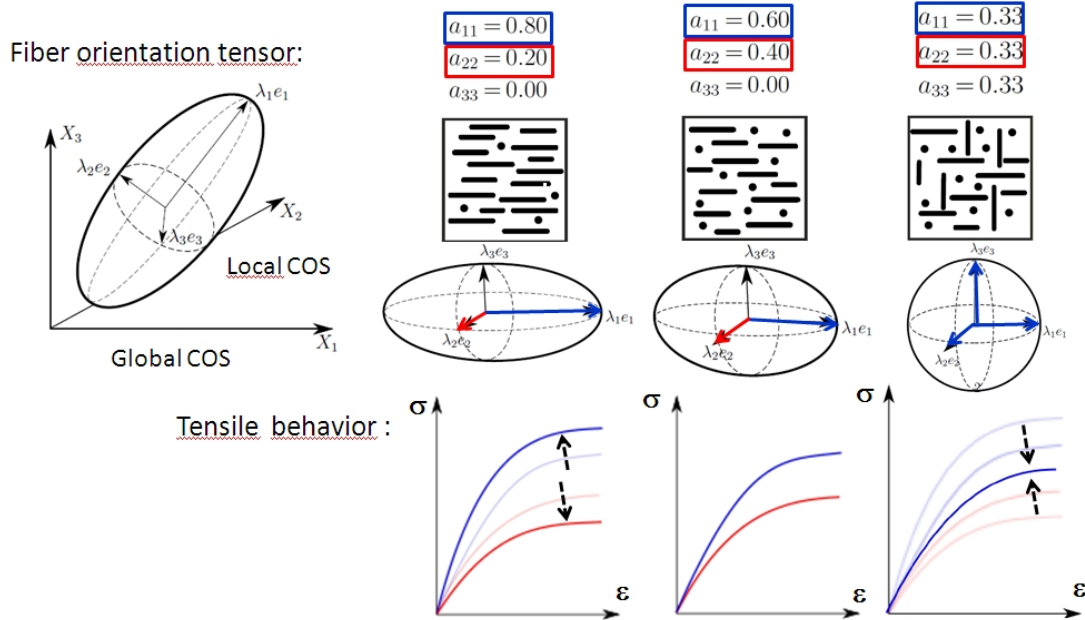


Fig. 14: Interpolation, respectively, extrapolation to unknown fiber orientation configurations.

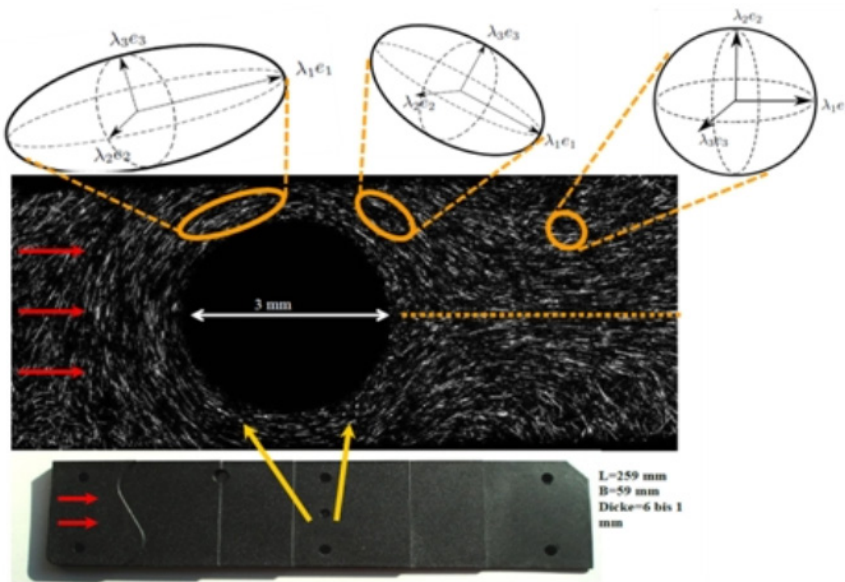


Fig. 15: Coordinate system free consideration of anisotropy: vectors of the preferred directions coincide with the principal directions of the fiber distribution tensor.

4.3 Quasi-static and dynamic $\pm 45^\circ$ tests of an organic sheet

The simulation results presented hereafter are obtained in a project with the Dr.Ing.h.c.F.Porsche AG. The organic sheet tested is a glass fiber fabric embedded in a polyamide matrix. The geometrical structure of the fabric and the exact denomination of the current organic sheet are confidential.

4.3.1 Material characterization

Before starting with the numerical modeling, the in-plane shear behavior has to be characterized based on the $\pm 45^\circ$ tests. The determination of the shear stresses and strains out of a $\pm 45^\circ$ test is given in the Technical Note DIN EN ISO 14129. The Technical Note does not regard the finite fiber rotations in the characterization. Furthermore, it is not clearly explained whether the true stresses or the technical stresses has to be used in the formulas given in the Technical Note DIN EN ISO 14129. The shear stresses and strains acc. DIN EN ISO 14129 read:

$$\begin{aligned}\tau_{12} &= \frac{1}{2}\sigma_x, \\ \gamma_{12} &= \varepsilon_x - \varepsilon_y\end{aligned}\quad (44)$$

In order to regard the finite fiber rotations, the rotation of the shear plane has to be considered in the characterization, see Fig.16. Furthermore, the **technical stresses** σ_x has to be inserted in the formulas (44) and (45), following a simple geometrical consideration (not explained here). Using the true stresses σ_x (as it is the “usual way” when using experimentally obtained hardening data), leads to completely wrong results!

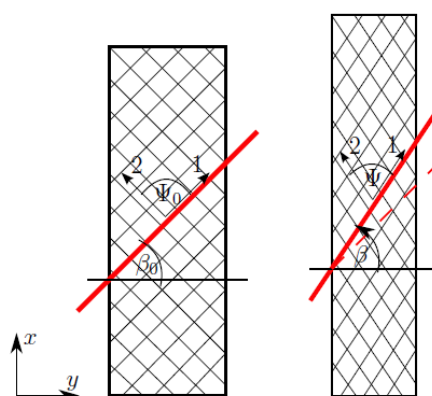


Fig. 16: Schematic representation of the $\pm 45^\circ$ tensile test: rotating shear plane due to finite fiber rotations

Hereafter, a characterization which regards the yarn rotations is proposed:

$$\begin{aligned}\tau_{12} &= \sigma_x \sin(\beta) \cos(\beta) \\ \gamma_{12} &= \varepsilon_x \sin(2\beta) - \varepsilon_y \sin(2\beta).\end{aligned}\quad (44)$$

The derived in-plane shear curve (shear stress – total strain) and the corresponding in-plane shear hardening curve is represented in Fig. 17.

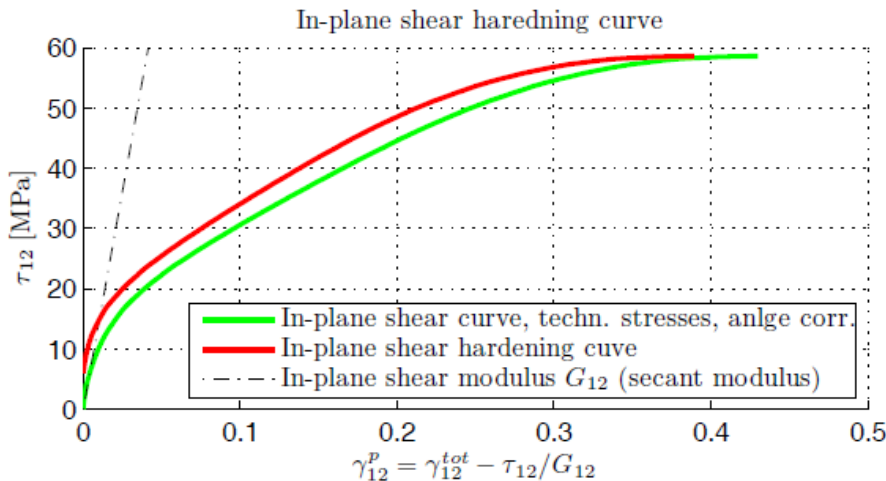


Fig. 17: Conversion from total stress-strain curve into shear hardening curve

4.3.2 Numerical modeling

At first, the effect of evolving anisotropy due to finite fiber rotations is studied numerically based on the simulation of single element tests. With these single element tests, also the influence of the additional anisotropy parameters (monoclinic anisotropy) is investigated and a physical interpretation of the parameters is given. These are in particular the parameter a_7 of the yield surface formulation (42) and the monoclinic elasticity parameter β_4 of the anisotropic elasticity law (23). Afterwards, the simulation of the material characterization tests is presented as a model verification.

For the simulation of the single-element tests, two cases are distinguished. In the first case (which is indicated with $irot=0$), the experimentally observed loading induced alignment of the yarns is not regarded. That is, during the load application the yarn angle Ψ does not change, i.e. $\Psi = \text{const.}$ holds during the whole loading process and the orientation of the vectors \mathbf{a} and \mathbf{b} does not change. In the second case (which is indicated with the option $irot=1$) the influence of finite fiber rotations is investigated and the vectors \mathbf{a} and \mathbf{b} are mapped with the deformation gradient \mathbf{F} . Furthermore, an initial yarn misalignment angle of $\Psi = 90^\circ$ is assumed in both cases, i.e. the vectors \mathbf{a} and \mathbf{b} representing the yarn directions are perpendicular to each other at the beginning of load application ($\mathbf{a} \perp \mathbf{b}$). That is, an ideal grid with orthogonally aligned yarns is assumed for the undeformed fabric and hence initial orthotropic behavior is provided. The two cases are summarized hereafter:

- $irot=0$: no fiber rotations, $\mathbf{a} \perp \mathbf{b}$ during load application ,
- $irot=1$: finite fiber rotations, \mathbf{a} and \mathbf{b} are mapped with \mathbf{F} , repectively, \mathbf{F}_p .

Fig. 18 shows a schematic representation of the modeling approaches with $irot=0$ (above) and $irot=1$. The modeling approach with the option $irot=1$ is more realistic, since it corresponds to the assumed deformation mechanisms of a fabric. Under tension, an alignment of the yarns in the load direction is observed whereas under compression the yarns deflect from the load direction. This leads to the observed stiffening effect in tension and the weakening effect in compression, as discussed hereafter.

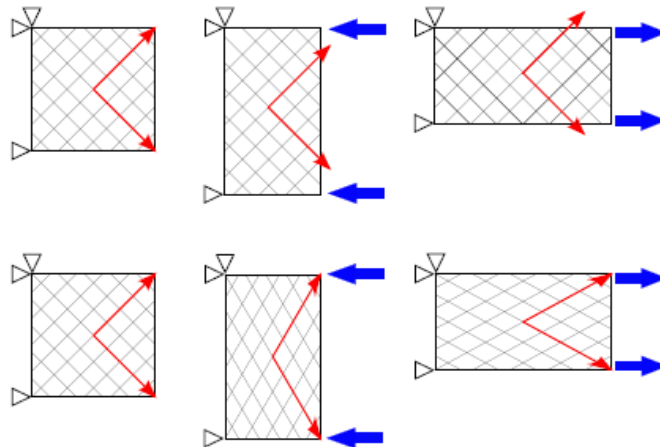


Fig. 18: Schematic representation of the modeling approaches with the option *irot=0* (no fiber rotation) and *irot=1* (finite fiber rotations). The yarn angle is Ψ .

In Fig. 19, the differences between the modeling approaches *irot=0* (no rotation of the yarns) and *irot=1* (finite fiber rotations) is studied at a single element test. The simulation with the option *irot=0* (rotation of yarns regarded) shows that both in compression and tension the pronounced nonlinear behavior can be predicted with the anisotropic material model. Furthermore, there is nearly no difference of the behavior in tension and in compression, the tension and the compression curves are almost symmetric with respect to the strain axis.

In contrast to that, the simulations with the option *irot=1* (finite fiber rotations regarded) show a significant difference between tension and compression. In case of uniaxial compression, the behavior is weaker compared to the simulations with *irot=0* and in the tensile tests the simulated stress-strain curve behaves stiffer compared to the option *irot=0*. Furthermore, an abrupt change of the slope of the tensile curve is observed at a strain value 0.22. After that “stiffening point”, the simulation of the tensile test performs much stiffer.

The weakening effect under compression and the stiffening effect under tension can be explained when considering again the sketch representing the deformation mechanisms of a fabric, see Fig. 18 (below). Under uniaxial compression, the yarn angle Ψ increases with ongoing deformations and the vectors **a** and **b** deflect from the line of the load application. The yarns are less aligned and, consequently, the yarns escape from the load transfer because of a bad angle. This results in pronounced yielding and the contribution of the yarns to the load transfer decreases with an increasing yarn angle Ψ . The opposite is observed under uniaxial tension. Due to the alignment of the yarns, the yarn angle Ψ decreases and the yarns are brought into line with the load direction. This promotes a load transfer into the fibers and, consequently, the fibers take over an increasing portion of the total load with ongoing deformations, which results in a stiffer behavior compared to the option *irot = 0*. The observed stiffness jump in the tensile stress - strain curve at the strain 0.22 can be identified as the point, where no further plastic deformations occur and the fiber carry all loads. That means that all deformations after 0.22 are purely elastic again and the applied load is stored as reversible elastic strain energy.

Finally, it can be concluded that with both options the experimentally observed highly non-linear behavior under shear dominated loadings can be simulated. However, the simulation with the option *irot=1* is more realistic, since the loading induced rotation of the yarns is considered and the stiffening effect in tension and the weakening effect in compression due to the yarn rotations are predicted realistically.

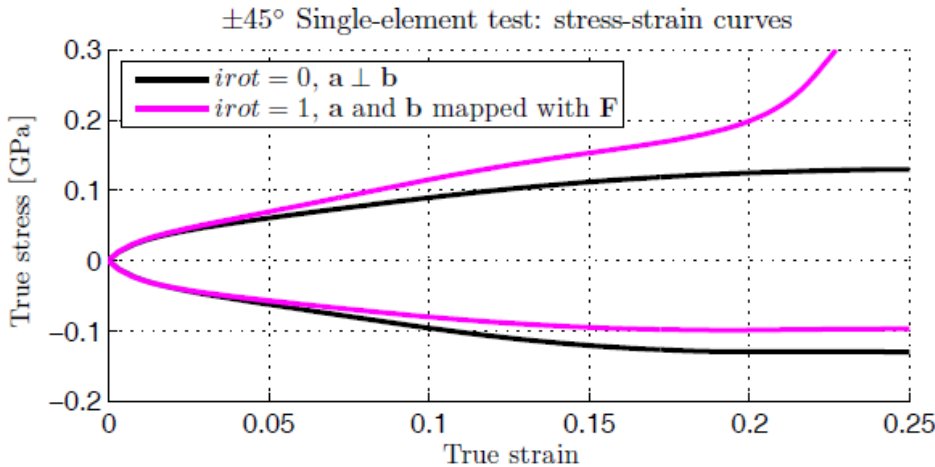


Fig. 19: $\pm 45^\circ$ single element tensile and compression test.

In a next step, the effect of the parameter α_7 and of the additional elastic parameter β_4 is studied. Here again, the parameter study is first performed at a single-element test. The objective is to study the qualitative influence of these parameters in order to get a physical meaning of the additional anisotropy parameters. Fig. 20 shows a variation of the yield surface parameter α_7 from 0 to -8 , while the elasticity parameters remain unchanged. It can be seen that the simulation curves with $irot=1$ have nearly a common intersection point. Before this intersection point, the difference between the simulations is not very distinct. However, after the intersection point, the difference between the varying parameters α_7 is significant.

Summarizing the observations it can be concluded that the influence of the parameter α_7 can be interpreted as a resistance of the matrix against rotation of the yarns. Up to a certain point, the so called stiffening point, the fibers carry all loads and no further plastic deformations occur. The parameter α_7 determines this stiffening point. With higher values for the parameter α_7 , the resistance against rotations of the yarns is higher and the point at which the fibers carry over all loads, i.e. the stiffening point, occurs earlier.

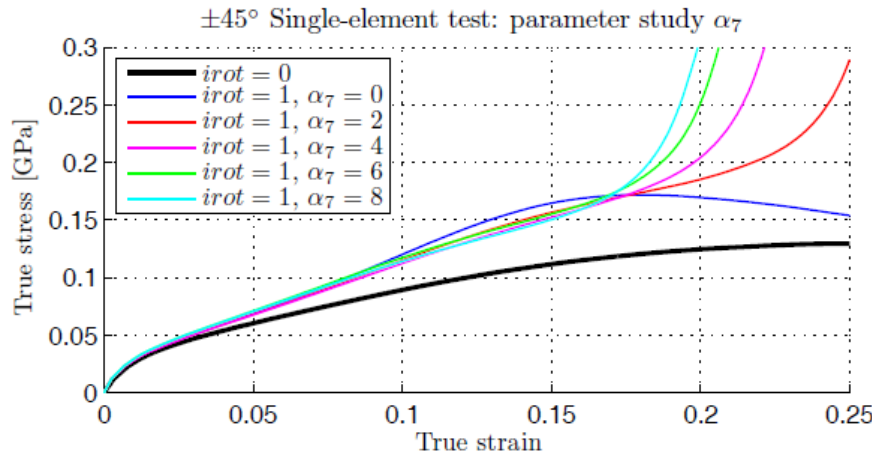


Fig. 20: Parameter study: effect of yield surface parameter α_7

Next, the influence of the anisotropic elasticity parameters β_4 is studied, while the parameter α_7 is left unchanged. Fig. 21 shows the simulations with varying elasticity parameters from $\beta_4 = 0$ to $\beta_4 = 20$. It can be seen that the stiffening point is nearly the same in all cases. Moreover, the behavior before the stiffening point doesn't show any significant differences in the predicted stress-strain curves. However, after the stiffening point, the simulated stress-strain curves show a significant dependency on the anisotropic elasticity parameters. The slope increases with decreasing parameters β_4 . Hence, the parameter β_4 determines the stiffness after the stiffening point is reached. That is, the monoclinic elasticity parameter β_4 accounts for the shear-normal interaction observed in monoclinic anisotropy. This is exactly the contribution highlighted in equations (23) and (24) (red color).

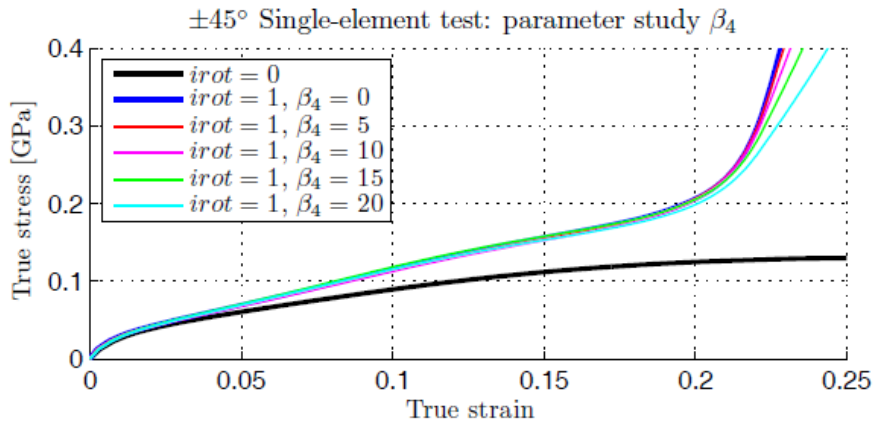


Fig. 21: Parameter study: effect of the monoclinic elasticity parameter β_4

Hereafter, the simulation of the material characterization tests is discussed. The simulation of the characterization tests represents a verification of the material model and of the proposed identification procedure.

Fig. 22 shows the simulation results of the $\pm 45^\circ$ tensile tests using the modeling options $irot=0$ and $irot=1$, whereby the yarn directions are mapped both with the total deformation gradient \mathbf{F} and with the plastic deformation gradient \mathbf{F}_p . In case the yarn directions are mapped with the total deformation gradient \mathbf{F} , the yarn rotation is overestimated resulting in a too stiff behavior. The best results are obtained when the vectors \mathbf{a} and \mathbf{b} are mapped with the plastic deformation gradient \mathbf{F}_p and if the yield surface parameter is set to $\alpha_7 = -6$. When interpreting the simulation results presented in Fig. 22, it seems to be a reasonable assumption that the rotations of the yarns follow the plastic deformations. Furthermore, the “stiffening point” seems to be the point at which final failure occurs. The failure mode observed can be identified as transverse tensile failure of the yarns in the organic sheet. This will be further investigated in an upcoming project.

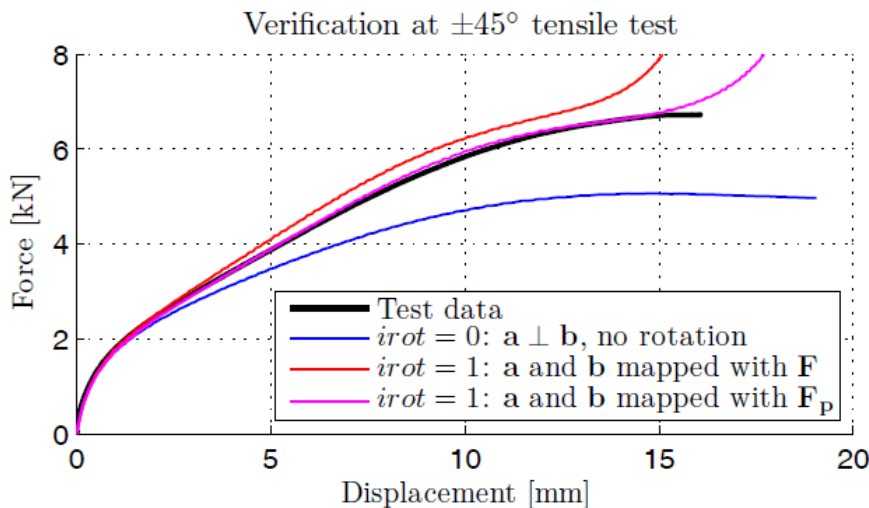


Fig. 22: Simulation results obtained with $irot=0$ and $irot=1$, \mathbf{a} and \mathbf{b} mapped with \mathbf{F} and with \mathbf{F}_p

Fig. 23 shows the simulation of the quasi-static and dynamic tensile tests, unfortunately just with the option $irot=0$ (no fiber rotations regarded). With the viscoplastic approach Eq. (27), the quasi static and the high speed tensile tests can be predicted sufficiently. The change in the elastic range (the viscoelastic behavior) is regarded by a simple scaling of the elasticity parameters.

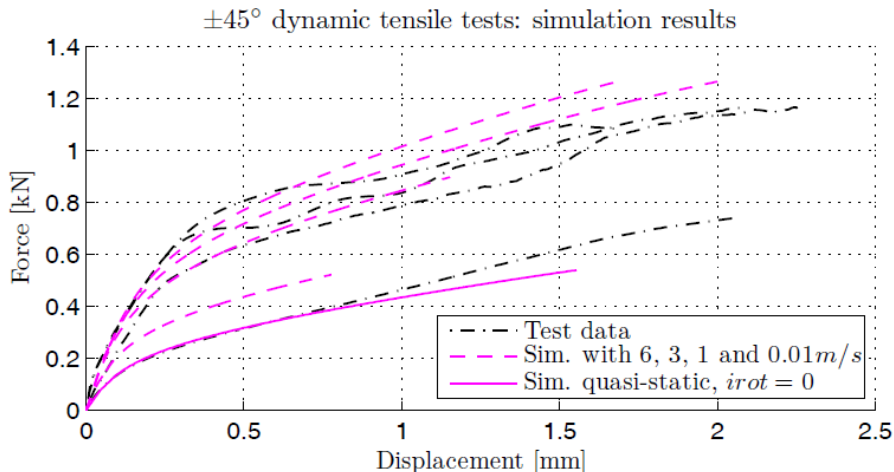


Fig. 23: Simulation of the quasi-static and dynamic $\pm 45^\circ$ tensile tests (option $irot=0$)

5 Summary and outlook

In this paper, new anisotropic constitutive models for short fiber reinforced thermoplastics, for unidirectional fiber reinforced polymers and for organic sheets were proposed. The models are able to predict the inelastic behavior of polymer composites under multi-axial loading conditions prior to the onset of failure. In order to describe and to model the pressure dependent inelastic behavior, an elastic-viscoplastic approach based on a non-associated flow rule is used. Furthermore, the plasticity models are based on a simple and straight forward model identification procedure using stress – plastic strain curves. That is, the experimentally obtained hardening curves in various stress states can be input as tabulated data into the material models. This allows a straight forward treatment of the experimentally obtained hardening data without any time consuming parameter identification. Furthermore, the non-associative flow rule enables the correct prediction of the plastic Poisson's ratios in various stress states. The Perzyna type viscoplastic formulation represents a simple and effective model in order to consider the strain rate dependent behavior in the plastic regime.

With respect to an industrial use of the proposed material model for organic sheets, the whole process chain from drape simulation to forming simulation and finally crash simulation will be addressed. The drape simulation gives the alignments of the yarns which have to be mapped as initial misalignments into the FE mesh. These initial misalignments can be directly regarded by the vectors **a** and **b** in the constitutive model. In a second step, the forming simulation predicts the loading induced misalignments. These loading induced misalignments due to the forming process can be mapped directly into the finite element mesh for the subsequent crash analysis.

For short fiber reinforced thermoplastics, the process chain mold flow simulation – crash simulation will be addressed. The fiber orientation tensor provided in the mold flow simulation can be directly used in the constitutive model. Further verification and validation of the proposed phenomenological modeling approach are required, including component tests.

For all the developed material models, extensions with respect to appropriate failure models and degradation laws have to be done. The proposed elastic-viscoplastic constitutive models can be used as a “constitutive basis” in order to add arbitrary failure criteria and degradation laws. Another important aspect is the coupling between viscoelasticity and viscoplasticity. Although the proposed scaling of the elasticity parameters represents a sufficient approach for crash analysis, a fully coupled viscoelastic-viscoplastic approach as proposed by [14] would be a more physically sound approach.

Acknowledgements

I would like to express my most sincere gratitude to Prof. Pedro Camanho (DEMEc - Faculdade de Engenharia, Universidade do Porto) and to Prof. Stefan Kolling (Institut für Mechanik und Materialforschung, Technische Hochschule Mittelhessen) for the long term support and for the encouragement of my research work. Furthermore, I would like to thank Dr. Hannes Körber (Institute

for Carbon Composites, Technische Universität München) for providing the experimental data for IM7-8552, for many fruitful discussions and for the very nice continuing collaboration. I would like to thank Dr. Julian Schöpfer (Dr.Ing.h.c.F.Porsche AG) for the nice collaboration and for many fruitful discussions. Furthermore, I have to thank Dr. Paulo Andrés Flores Vega (Department of Mechanical Engineering, Universidad de Concepción, Chile) for fruitful discussions and for the upcoming projects. I would like to thank Prof. Raimund Rolfes (Institute of Structural Analysis, Leibniz Universität Hannover) for offering me the possibility to write a phd thesis and for supporting my research work. Last but not least I have to thank DYNAmore GmbH for the support and for providing the LS-DYNA licenses.

6 Literature

- [1] M. Vogler, G. Ernst and R. Rolfes "Invariant based transversely-isotropic material and failure model for fiber-reinforced polymers." *Computers, Materials & Continua*, Vol. 16, No. 1, pp 25-49, 2010.
- [2] M. Vogler, R. Rolfes and P.P. Camanho "Modeling the inelastic deformation and fracture of polymer composites – part I: plasticity model." *Mechanics of Materials*, Submitted for publication, 2012.
- [3] Vogler M., Andrade, F., Schöpfer, J., Kolling, S. & Rolfes, R. (2011, 23 - 24 May). A novel transversely-isotropic 3D elastic-viscoplastic constitutive law for modeling fiber matrix composites [Conference Proceedings, Download: www.dynalook.com/]. In 8th European LS-DYNA Users Conference. Strasbourg, France.
- [4] P.P. Camanho, M. Bessa, G. Catalanotti, M. Vogler "Modeling the inelastic deformation and fracture of polymer composites – part II: smeared crack model." *Mechanics of Materials*, Submitted for publication, 2012.
- [5] Pae, K., & Rhee, K., Effects of hydrostatic pressure on the compressive behavior of thick laminated 45° and 90° unidirectional graphite-fiber/epoxy-matrix composites. *Composites Science and Technology*, 53(3), 281 – 287, 1995.
- [6] H. Koerber, J. Xavier and P.P. Camanho "High strain rate characterization of unidirectional carbon-epoxy IM7-8552 in transverse compression and in-plane shear using digital image correlation." *Mechanics of Materials*, 42(11), 1004 – 1019.
- [7] J. Schröder "Theoretische und algorithmische Konzepte zur phänomenologischen Beschreibung anisotropen Materialverhaltens." Phd thesis, Universität Hannover, 1995.
- [8] Ebbing, Vera. Design of polyconvex energy functions for all anisotropy classes. Inst. für Mechanik, Abt. Bauwissenschaften, 2010.
- [9] A. Spencer "Kinematic constraints, constitutive equations and failure rules for anisotropic materials." In J. Boehler (Ed.), "Applications of tensor functions in solid mechanics." (pp. 187-201). Springer, 1987.
- [10] F. K. Chang, K.-Y. Chang "A progressive damage model for laminated composites containing stress concentrations." *Journal of Composite Materials*, 21(9), 834-855, 1987.
- [11] P. Maimi, P.P. Camanho, J. Mayugo and A. Turon "Matrix cracking and delamination in laminated composites. Part I: Ply constitutive law, first ply failure and onset of delamination. *Mechanics of Materials*, 43(4), 169 – 185, 2011.
- [12] ten Thije, R.H.W., Akkermann, R. & Huétink, J. "Large deformation simulation of anisotropic material using an updated lagrangian finite element method." *Computer Methods in Applied Mechanics and Engineering*, 196(33–34), 3141–3150, 2007
- [13] Huétink, J. "On anisotropy, objectivity and invariancy in finite thermo-mechanical deformations" in: Proceedings on the 9th International ESAFORM Conference on Material Forming, Publishing House Akapit, Krakow, Poland, ISBN 83-89541-66-1, pp. 355–358, 2006
- [14] Launay, A., Maitournam, M., Marco, Y., Raoult, I., & Szmytka, F. (2011). "Cyclic behaviour of short glass fibre reinforced polyamide: Experimental study and constitutive equations." *International Journal of Plasticity*, 27 (8), 1267 - 1293.
- [15] Badel, P., Gauthier, S., Vidal-Sallé, E., & Boisse, P. "Rate constitutive equations for computational analyses of textile composite reinforcement mechanical behavior during forming." *Composites Part A: Applied Science and Manufacturing*, 40(8), pp. 997–1007, 2009